Evaluation on the impact of IMU grades on BDS + GPS PPP/INS tightly coupled integration

Zhouzheng Gao [a,b,c,d,*], Maorong Ge [d], Wenbin Shen [b], You Li [e], Qijin Chen [c], Hongping Zhang [c], Xiaoji Niu [c]

[a] School of Land Science and Technology, China University of Geosciences, 29 Xueyuan Road, Beijing 100083, China
[b] School of Geodesy and Geomatics, Wuhan University, 129 Luoyu Road, Wuhan 430079, China
[c] GNSS Research Center, Wuhan University, 129 Luoyu Road, Wuhan 430079, China
[d] German Research Centre for Geosciences (GFZ), Telegrafenberg, Potsdam 14473, Germany
[e] Department of Geomatics Engineering, The University of Calgary, 2500 University Dr. N.W., Calgary, Alberta T2N 1N4, Canada

Abstract

The unexpected observing environments in dynamic applications may lead to partial and/or complete satellite signal outages frequently, which can definitely impact on the positioning performance of the Precise Point Positioning (PPP) in terms of decreasing available satellite numbers, breaking the continuity of observations, and degrading PPP's positioning accuracy. Generally, both the Inertial Navigation System (INS) and the multi-constellation Global Navigation Satellite System (GNSS) can be used to enhance the performance of PPP. This paper introduces the mathematical models of the multi-GNSS PPP/INS Tightly Coupled Integration (TCI), and investigates its performance from several aspects. Specifically, it covers (1) the use of the BDS/GPS PPP, PPP/INS, and their combination; (2) three positioning modes including PPP, PPP/INS TCI, and PPP/INS Loosely Coupled Integration (LCI); (3) the use of four various INS systems named navigation grade, tactical grade, auto grade, and Micro-Electro-Mechanical-Sensors (MEMS) one; (4) three PPP observation scenarios including PPP available, partially available, and fully outage. According to the statistics results, (1) the positioning performance of the PPP/INS (either TCI or LCI) mode is insignificantly depended on the grade of inertial sensor, when there are enough available satellites; (2) after the complete GNSS outages, the TCI mode expresses both higher convergence speed and more accurate positioning solutions than the LCI mode. Furthermore, in the TCI mode, using a higher grade inertial sensor is beneficial for the PPP convergence; (3) under the partial GNSS outage situations, the PPP/INS TCI mode position divergence speed is also restrained significantly; and (4) the attitude determination accuracy of the PPP/INS integration is highly correlated with the grade of inertial sensor.
© 2017 COSPAR. Published by Elsevier Ltd. All rights reserved.

Keywords: Precise Point Positioning (PPP); BeiDou Navigation Satellite System (BDS); Inertial Navigation System (INS); PPP/INS Tightly Coupled Integration (TCI)

1. Introduction

Since the theoretical model of the integration between the Global Positioning System (GPS) and the Inertial Navigation System (INS) was proposed by Cox (1978), such integration method has been used as a precise positioning tool in many dynamic positioning applications, especially when the GPS Real-time Kinematic (RTK) technology

* Corresponding author at: School of Land Science and Technology, China University of Geosciences, 29 Xueyuan Road, Beijing 100083, China.

E-mail addresses: zhouzhenggao@126.com (Z. Gao), maor@gfz-potsdam.de (M. Ge), wbshen@sgg.whu.edu.cn (W. Shen), liyou331@gmail.com (Y. Li), chenqijin@whu.edu.cn (Q. Chen), hpzhang@whu.edu.cn (H. Zhang), xjniu@whu.edu.cn (X. Niu).

(Kim et al., 1998; Scherzinger, 2000) has been invented. However, GPS RTK has some inherent limitations. Besides the costliness in operation due to the requirement of a base station, the performance of RTK degrades dramatically along with the increasing distance between the base station and the user. Such drawbacks have limited the application of RTK/INS integration, especially for the mass-market applications.

Fortunately, the Precise Point Positioning (PPP) method proposed by Zumberge et al. (1997) can overcome the disadvantages of RTK by processing dual-frequency GPS observations with the aids of the precise satellite orbit and clock products (Kouba, 2009) from the International Global Navigation Satellite System (GNSS) Service (IGS, Dow et al., 2009). Benefiting from the development of the PPP related algorithms in recent years, such as the raw observations based PPP model (Geng et al., 2011; Tu et al., 2013), and ambiguity resolution PPP (Ge et al., 2008; Bertiger et al., 2010; Li et al., 2013), PPP has been applied diffusely in displacement monitoring (Li et al., 2013, 2014) and meteorology prediction (Lu et al., 2015). However, it is still challenging to introduce the PPP to the dynamic precise positioning application, particularly in the city canyon land-borne applications. Generally, there are two major reasons. Firstly, PPP needs a long time to assure the ambiguity researching a constant (Zhang et al., 2013). Besides, the GPS signal tracking might be partially or completely broken frequently, which leads to the re-initialization procedure in the PPP calculation and degrades its positioning accuracy (Zhang and Li, 2012; Gao et al., 2015).

To improve the performance of PPP, the integration model between PPP and INS has been proposed (Zhang and Gao, 2008). According to the previous studies of Roesler and Martell (2009), the kinematic performance of GPS PPP in terms of positioning accuracy, reliability, and continuity can be improved significantly in both the challenging conditions and the open sky environments, when aided by either navigation or tactical grade INS sensors. Along with the development of the Micro-Electro-Mechanical-Sensors (MEMS) technology, the integration between PPP and MEMS INS has been studied (Rabbou and El-Rabbany, 2015; Gao et al., 2016), which makes it possible to use the PPP/INS integration systems in the mass market with low-cost sensors. Meanwhile, according to the study of Du and Gao (2012), INS can aid the un-differential cycle slip detection in PPP data pre-processing. Moreover, from the research of Gao et al. (2016), both the convergence speed and the re-convergence time of PPP can be shortened significantly by introducing the INS. However, the magnitudes of sensor errors vary significantly for different grades of INS sensors. Various grades of INS sensors lead to different INS navigation performances significantly. However, for the PPP/INS integration, there is a possibility that even with different grades of INS, one may obtain similar level of performance. Thus, if one can obtain a required accuracy with a lower grade INS, it is not necessary to use a higher one, because the cost of different grade IMUs are significantly different (*e.g.*, $ 1 million level for a navigation grade INS, $ 10 thousand level for a tactical one, etc.).

On the other hand, the absolute positioning accuracy of the PPP/INS integration is largely impacted by PPP. This is because in such integration, PPP provides long-term absolute position updates, while the INS algorithm smooths and denoises the results when PPP is available, and bridges the PPP outages in some challenging circumstances. Thus, it can also enhance the PPP performance. According to the previous studies (Yang et al., 2011; Odijk et al., 2015; Pan et al., 2015; Chen et al., 2016), the combination of the GPS and the BeiDou Navigation Satellite System (BDS) can enhance the PPP performance in terms of providing more available satellites, smaller Position Dilution Of Precision (PDOP), rapider convergence speed, and better positioning accuracy and continuity in the whole Asia-pacific region. The use of such multi-constellation GNSS is a trend for both professional and mass-market applications.

Generally speaking, to enhance the performance of PPP, there are general two approaches: using multi-GNSS data, and integrating PPP with other sensors (*i.e.* INS). To investigate on the contribution of these methods, this paper introduces the mathematical models of the BDS + GPS PPP/INS Tightly Coupled Integration (TCI), including the BDS + GPS raw PPP models, INS mechanization, and the observation models and the state models of the PPP/INS integration. Meanwhile, this paper implements various land-borne tests to validate the final performance of the introduced algorithms, and it is organized as follows. Section 2 is the methodology part, which illustrates the mathematical models for PPP, INS, and their integration. Section 3 demonstrates the implementation, tests, and results, including the experiment descriptions, positioning performance, and attitude determination performance. Finally, Section 4 draws the conclusions. Comparing with the previous works, it is a more systemic research. Specifically, it investigates: (1) The use of multi-GNSS PPP (*i.e.*, BDS + GPS), PPP/INS, and their combination in dynamic applications. In particular PPP, GPS only, BDS only, and BDS + GPS are compared; (2) Three positioning modes, that is, PPP, PPP/INS TCI, and the PPP/INS Loosely Coupled Integration (LCI); (3) The use of four various INS systems, which covers all possible grades of INS, that is, navigation grade, tactical grade, auto grade, and low-cost MEMS one; (4) Three PPP observation scenarios, including PPP available, partially available, and fully outage. Moreover, there are some new outcomes from this research.

2. Methodology of PPP/INS integration

In this section, the mathematical models for PPP using raw observations of BDS and GPS are firstly provided, followed by the PPP/INS integration observation model and

the state model. Afterwards, the detailed INS models are also illustrated.

2.1. BDS+GPS raw precise point positioning model

In the raw PPP model, the positioning observation functions of BDS and GPS can be expressed respectively as (Zhang et al., 2013)

$$
\begin{pmatrix} P_j^B \\ L_j^B \end{pmatrix} = \begin{pmatrix} \|\boldsymbol{p}^B - \boldsymbol{p}_r\| + c(t_r - t^B) + d_{r,j}^B - d_j^B + T_r^B + I_{r,j}^B + \Delta P_{r,j}^B \\ \|\boldsymbol{p}^B - \boldsymbol{p}_r\| + c(t_r - t^B) + \lambda_j^B(N_{r,j}^B + u_{r,j}^B - u_j^B) + T_r^B - I_{r,j}^B + \Delta L_{r,j}^B \end{pmatrix}
$$
$$
+ \begin{pmatrix} \varepsilon_{Pr,j}^B \\ \varepsilon_{Lr,j}^B \end{pmatrix}, \begin{pmatrix} \varepsilon_{Pr,j}^B \\ \varepsilon_{Lr,j}^B \end{pmatrix} \sim N \begin{pmatrix} 0, \sigma_{Pr^B}^2 \\ 0, \sigma_{Lr^B}^2 \end{pmatrix} \tag{1}
$$

$$
\begin{pmatrix} P_j^G \\ L_j^G \end{pmatrix} = \begin{pmatrix} \|\boldsymbol{p}^G - \boldsymbol{p}_r\| + c(t_r - t^G) + d_{r,j}^G - d_j^G + T_r^G + I_{r,j}^G + \Delta P_{r,j}^G \\ \|\boldsymbol{p}^G - \boldsymbol{p}_r\| + c(t_r - t^G) + \lambda_j^G(N_{r,j}^G + u_{r,j}^G - u_j^G) + T_r^G - I_{r,j}^G + \Delta L_{r,j}^G \end{pmatrix}
$$
$$
+ \begin{pmatrix} \varepsilon_{Pr,j}^G \\ \varepsilon_{Lr,j}^G \end{pmatrix}, \begin{pmatrix} \varepsilon_{Pr,j}^G \\ \varepsilon_{Lr,j}^G \end{pmatrix} \sim N \begin{pmatrix} 0, \sigma_{Pr^G}^2 \\ 0, \sigma_{Lr^G}^2 \end{pmatrix} \tag{2}
$$

and the corresponding velocity functions can be written as (Gao et al., 2015)

$$
\begin{pmatrix} D_j^B \lambda_j^B \\ D_j^G \lambda_j^G \end{pmatrix} = \begin{pmatrix} \|\boldsymbol{v}^B - \boldsymbol{v}_r\| + c(\dot{t}_r - \dot{t}^B) \\ \|\boldsymbol{v}^G - \boldsymbol{v}_r\| + c(\dot{t}_r - \dot{t}^G) \end{pmatrix} + \begin{pmatrix} \varepsilon_{Dr,j}^B \\ \varepsilon_{Dr,j}^G \end{pmatrix},
$$
$$
\begin{pmatrix} \varepsilon_{Dr,j}^B \\ \varepsilon_{Dr,j}^G \end{pmatrix} \sim N \begin{pmatrix} 0, \sigma_{Dr^B}^2 \\ 0, \sigma_{Dr^G}^2 \end{pmatrix} \tag{3}
$$

where the subscripts j and r represent the signal frequency (BDS: B_1 and B_2; GPS: L_1 and L_2) and receiver; the superscripts B and G refer to BDS and GPS systems; P, L, and D denote the raw observations of pseudo-range, carrier-phase, and Doppler, respectively; $\boldsymbol{p}^B$ ($\boldsymbol{p}^G$) and $\boldsymbol{v}^B$ ($\boldsymbol{v}^G$) stand for the position and velocity of BDS (GPS) satellite at the antenna phase center after the satellite PCO (phase center offset) corrections (Ge et al., 2005); $\boldsymbol{p}_r$ and $\boldsymbol{v}_r$ indicate the position and velocity at receiver antenna phase center, also without receiver PCO impact; t_r and $\dot{t}_r$ are the offset and drift of receiver clock; t^B (t^G) and $\dot{t}^B$ ($\dot{t}^G$) represent the BDS (GPS) satellite clock bias and drift; d_r^B (d_r^G) and d^B (d^G) stand for the hardware time delays of receiver and satellite on the pseudo-range (Tu et al., 2013; Zhang et al., 2013); u_r^B (u_r^G) and u^B (u^G) stand for the hardware time delays of receiver and satellite on the carrier-phase, which can be absorbed by the ambiguity (Ge et al., 2008; Li et al., 2013); T and I denote the tropospheric delay and ionospheric delay along the signal transmitting path; ΔP and ΔL are the sum of the error corrections for pseudo-range and carrier-phase (Witchayangkoon, 2000); λ and N represent the wavelength and the integer ambiguity; c and ε are the velocity of light in vacuum and the observation noise. Empirically, the priori covariance values for the observation noise of pseudo-range, carrier-phase, and Doppler can be 30 cm, 3 mm, and 10 cm/s, respectively. In order to make the priori covariance of each observation with different satellite elevation angle satisfy the real situation as much as possible, the satellite elevation angle

dependent model (Gendt et al., 2003) is utilized. Besides, due to the orbit determination accuracy of BDS Geosynchronous Earth Orbit (GEO) satellites are about 1.5–2.5 times lower than that of other satellites (Steigenberger et al., 2012; Zhao et al., 2013), the priori covariance of GEO observations will be degraded in the data process.

Usually, most of the errors in Eqs. (1) and (2) can be corrected by the classic models (Witchayangkoon, 2000) and IGS products (Kouba, 2009). In the raw PPP model, the ionospheric delay and the pseudo-range hardware time delay, which can be mitigated using the ionosphere free combination (Zumberge et al., 1997), are estimated as parameters together with the residual of the zenith total delay of tropospheric wet component (WZTD) (Tu et al., 2013; Zhang et al., 2013). However, the parameterization of ionospheric delay for each satellite may weaken the solutions of the raw PPP. To strengthen the solutions, the apriori constraint on the slant ionospheric delay is adopted

$$
I_{r,1}^s = 40.28 \cdot STEC / f_{s,1}^2 \tag{4}
$$

where s refers to satellite system (B and G); $STEC$ is total electronic constant along the slant signal path, which can be achieved from Global Ionosphere Maps (GIM) (Schaer et al., 1998). Then, the temporal change of the ionospheric delay and the pseudo-range hardware time delay can be modelled as a random walk process

$$
\begin{pmatrix} I_{r,1,k}^s \\ d_{r,1,k}^s \end{pmatrix} = \begin{pmatrix} I_{r,1,k-1}^s \\ d_{r,1,k-1}^s \end{pmatrix} + \begin{pmatrix} \omega_{I,1,k-1}^s \\ \omega_{d,1,k-1}^s \end{pmatrix},
$$
$$
\begin{pmatrix} \omega_{I,1,k-1}^s \\ \omega_{d,1,k-1}^s \end{pmatrix} \sim N \begin{pmatrix} (0, \sigma_I^2) \\ (0, \sigma_d^2) \end{pmatrix} \tag{5}
$$

where σ_I^2 and σ_d^2 are the priori variance of the state noise of ionospheric delay ($\omega_{I,r,1}^s$) and pseudo-range hardware time delay ($\omega_{d,r,1}^s$) at frequency 1, which can be described using the temporal and spatial relative model introduced by Tu et al. (2013) and Zhang et al. (2013). Meanwhile, the corresponding values at frequency 2 can be expressed by

$$
\begin{pmatrix} I_{r,2}^s \\ d_{r,2}^s \end{pmatrix} = \kappa^s \begin{pmatrix} I_{r,1}^s \\ d_{r,1}^s \end{pmatrix} + \begin{pmatrix} \omega_{I,2,k-1}^s \\ \omega_{d,2,k-1}^s \end{pmatrix},
$$
$$
\begin{pmatrix} \omega_{I,2,k-1}^s \\ \omega_{d,2,k-1}^s \end{pmatrix} \sim N \begin{pmatrix} (0, (\kappa^s)^2 \sigma_I^2) \\ (0, (\kappa^s)^2 \sigma_d^2) \end{pmatrix}, \quad \kappa^s = f_{s,1}^2 / f_{s,2}^2 \tag{6}
$$

where $d_{r,1}^s$ and $d_{r,2}^s$ are the receiver hardware time delay at frequencies 1 and 2 on the pseudo-range. Due to the different signal structures and frequencies adopted by BDS and GPS, the value of $d_{r,1}^G$ and $d_{r,1}^B$ are usually different even for the same receiver. Such difference is named the inter-system bias (Gao et al., 2016), which can be defined as

$$
\Delta d_{r,1}^{B,G} = d_{r,1}^B - d_{r,1}^G \tag{7}
$$

where $\Delta d_{r,1}^{B,G}$ is the inter-system bias between BDS and GPS which can be parameterized as a random walk process.

Finally, the state parameter vector of the BDS + GPS raw PPP can be written as

$$X = \left[\delta \boldsymbol{p}_r, \delta \boldsymbol{v}_r, \delta t_r, \delta \dot{t}_r, \delta d_{r,1}^B, \delta d_{r,1}^G, \delta d_{wztd}, \delta \boldsymbol{N}_1^B, \delta \boldsymbol{N}_2^B, \delta \boldsymbol{N}_1^G, \delta \boldsymbol{N}_2^G, \delta \boldsymbol{I}_1^B, \delta \boldsymbol{I}_1^G\right]^T \tag{8}$$

where δ denotes the correction value; d_{wztd} is the residual of the zenith total delay of the tropospheric wet component. Then, either Kalman filter or sequential least square (Martin and George, 1981; Brown and Hwang, 1997) can be utilized to estimate the parameters in Eq. (8).

2.2. Observation models of BDS + GPS PPP/INS integration

There are two types of models for the PPP/INS integration system, including the observation models and the state models. The former are updates from PPP, while the latter are information obtained by using the INS predictions. The observation and state models are described in the current and next subsection, respectively.

In general, the observation function of both the tightly coupled integration (TCI) and the loosely coupled integration (LCI) (Godha, 2006) can be expressed uniformity as

$$\boldsymbol{Z}_k = \boldsymbol{H}_k \boldsymbol{X}_k + \boldsymbol{\eta}_k, \boldsymbol{\eta}_k \sim (0, \boldsymbol{R}_k) \tag{9}$$

where $\boldsymbol{Z}$ and $\boldsymbol{H}$ indicate the innovation vector and the designed coefficient matrix of the state parameter vector $(\boldsymbol{X})$ in Kalman filter at epoch k; $\boldsymbol{\eta}_k$ represents the observations noise with the apriori variance of $\boldsymbol{R}_k$, which is usually assumed to be a Gauss normal distribution.

In the TCI mode, the raw BDS/GPS observations and the INS predicted carrier-phase, pseudo-range, and Doppler values are utilized to form the innovation vector in Eq. (9), which can be written as

$$\boldsymbol{Z}_{TCI,k} = \begin{pmatrix} P_j^B \\ L_j^B \\ D_j^B \lambda_j^B \\ P_j^G \\ L_j^G \\ D_j^G \lambda_j^G \end{pmatrix} - \begin{pmatrix} P_{j,INS}^B \\ L_{j,INS}^B \\ \dot{P}_{j,INS}^B \\ P_{j,INS}^G \\ L_{j,INS}^G \\ \dot{P}_{j,INS}^G \end{pmatrix}$$

$$= \begin{pmatrix} P_j^B - (\|\boldsymbol{p}^B - \boldsymbol{p}_{r,INS} - \Delta \boldsymbol{p}_{r,\iota}\| + c(t_r - t^B) + d_{r,j}^B - d_j^B + T_r^B + I_{r,j}^B + \Delta P_{r,j}^B) \\ L_j^B - (\|\boldsymbol{p}^B - \boldsymbol{p}_{r,INS} - \Delta \boldsymbol{p}_{r,\iota}\| + c(t_r - t^B) + \lambda_j^B \tilde{N}_{r,j}^B + T_r^B - I_{r,j}^B + \Delta L_{r,j}^B) \\ D_j^B \lambda_j^B - (\|\boldsymbol{v}^B - \boldsymbol{v}_{r,INS} - \Delta \boldsymbol{v}_{r,\iota}\| + c(\dot{t}_r - \dot{t}^B)) \\ P_j^G - (\|\boldsymbol{p}^G - \boldsymbol{p}_{r,INS} - \Delta \boldsymbol{p}_{r,\iota}\| + c(t_r - t^G) + d_{r,j}^G - d_j^G + T_r^G + I_{r,j}^G + \Delta P_{r,j}^G) \\ L_j^G - (\|\boldsymbol{p}^G - \boldsymbol{p}_{r,INS} - \Delta \boldsymbol{p}_{r,\iota}\| + c(t_r - t^G) + \lambda_j^G \tilde{N}_{r,j}^G + T_r^G - I_{r,j}^G + \Delta L_{r,j}^G) \\ D_j^G \lambda_j^G - (\|\boldsymbol{v}^G - \boldsymbol{v}_{r,INS} - \Delta \boldsymbol{v}_{r,\iota}\| + c(\dot{t}_r - \dot{t}^G)) \end{pmatrix} \tag{10}$$

In the LCI mode, the position and velocity obtained from the BDS/GPS PPP mode and those from the INS mechanization are used to form the innovation vector, which can be expressed as

$$\boldsymbol{Z}_{LCI,k} = \begin{pmatrix} \boldsymbol{p}_r \\ \boldsymbol{v}_r \end{pmatrix} - \begin{pmatrix} \boldsymbol{p}_{r,INS} \\ \boldsymbol{v}_{r,INS} \end{pmatrix} - \begin{pmatrix} \Delta \boldsymbol{p}_{r,\iota} \\ \Delta \boldsymbol{v}_{r,\iota} \end{pmatrix} + \begin{pmatrix} \boldsymbol{\eta}_p \\ \boldsymbol{\eta}_v \end{pmatrix},$$
$$\begin{pmatrix} \boldsymbol{\eta}_p \\ \boldsymbol{\eta}_v \end{pmatrix} \sim N \begin{pmatrix} 0, \sigma_p^2 \\ 0, \sigma_v^2 \end{pmatrix} \tag{11}$$

where the "INS" stands for the INS predicted values; $\tilde{N}$ is the float ambiguity; $\boldsymbol{p}_r$, and $\boldsymbol{v}_r$ are the position and velocity at receiver antenna phase center calculated by BDS/GPS observations; $\boldsymbol{p}_{r,\ INS}$ and $\boldsymbol{v}_{r,\ INS}$ refer to the position and velocity at the Inertial Measurement Unit (IMU) measuring center predicted by INS mechanization (Savage, 2000; Shin, 2006); σ_p^2 and σ_v^2 are the priori covariance for the position innovation and velocity innovation, which are usually achieved from the PPP calculations directly, as mentioned above, the priori covariance for Eq. (10) can be obtained according to Eqs. (1)–(3); $\Delta \boldsymbol{p}_{r,\iota}$ and $\Delta \boldsymbol{v}_{r,\iota}$ represent the corrections for the lever-arm offset between the measuring centers of BDS/GPS receiver and that of IMU, with the correction expressions of

$$\begin{pmatrix} \Delta \boldsymbol{p}_{r,\iota} \\ \Delta \boldsymbol{v}_{r,\iota} \end{pmatrix} = \boldsymbol{C}_n^e \begin{pmatrix} \boldsymbol{C}_b^n \boldsymbol{\iota}^b \\ (\boldsymbol{\omega}_{in}^n \times) \boldsymbol{C}_b^n \boldsymbol{\iota}^b - \boldsymbol{C}_b^n (\boldsymbol{\iota}^b \times) \boldsymbol{\omega}_{ib}^b \end{pmatrix} \tag{12}$$

where the subscripts i, e, n, and b represent the inertial frame, Earth-Centered-Earth-Fixed (ECEF) frame (e.g., WGS84), navigation frame (e.g., North-East-Down), and body frame (x-y-z axes of inertial sensors, e.g., Forward-Right-Down), respectively; $\boldsymbol{C}_n^e$ is the transition matrix between the e frame and the n frame; $\boldsymbol{C}_b^n$ indicates the transition matrix between the n frame and the b frame; $\boldsymbol{\iota}^b$ is the lever-arm values measured accurately in the b frame before the system operating; $\boldsymbol{\omega}_{in}^n$ denotes the rotation angular rates of the n frame with respect to the i frame, projected in the n frame; $\boldsymbol{\omega}_{ib}^b$ stands for the angular rate output from the triaxial gyroscopes (g), which are assumed mainly affected by the biases $(\boldsymbol{B})$ and the scale factor errors $(\boldsymbol{S})$

$$\boldsymbol{\omega}_{ib}^b = (\boldsymbol{I} + \boldsymbol{S}_g)\hat{\omega}_{ib}^b + \boldsymbol{B}_g \Delta t + \varepsilon_g \tag{13}$$

similarly, the specific force output from the triaxial accelerometers (a) can be expressed as

$$\boldsymbol{f}^b = (\boldsymbol{I} + \boldsymbol{S}_a)\hat{\boldsymbol{f}}^b + \boldsymbol{B}_a \Delta t + \varepsilon_a \tag{14}$$

where $\boldsymbol{I}$ and Δt denote the unit matrix and the time interval between two adjacent IMU epochs; $\hat{\omega}_{ib}^b$ and $\hat{\boldsymbol{f}}^b$ are the theoretical values of angular rates and specific force; ε_a and ε_g represent the measurement noises of accelerometers and gyroscopes.

The designed coefficient matrix of both the TCI and LCI modes can be obtained by making the differential operation on Eqs. (10) and (11) after considering Eqs. (12)–(14). The used state vector and state models are described in the following subsection.

2.3. State models of BDS+GPS PPP/INS integration

The state dynamic function for GNSS/INS integration system can be expressed as

$$X_k = \Phi_{k/k-1}X_{k-1} + \mu_{k-1}, \mu_{k-1} \sim N(0, Q_{k-1}) \qquad (15)$$

where Φ is the state transition matrix from epoch k-1 to k, which is determined directly by the dynamic models adopted to describe the dynamic behavior of each parameter; μ_k denotes the state parameter noise with the apriori variance of Q_{k-1} and its values are mainly determined by the accuracy of the state dynamic model and the performance of IMU sensors (as shown in Table 1).

For the TCI mode, the corresponding state parameter vector can be written as

$$X_{TCI} = \left[\delta p_r, \delta v_r, \delta\theta, \delta B_a, \delta S_a, \delta B_g, \delta S_g, \delta t_r, \delta\dot{t}_r, \delta d_{r,1}^B, \delta d_{r,1}^G, \delta d_{wztd}, \delta N_1^B, \delta N_2^B, \delta N_1^G, \delta N_2^G, \delta I_1^B, \delta I_1^G \right]^T \qquad (16)$$

and the state parameter vector of the LCI mode is

$$X_{LCI} = \left[\delta p_r, \delta v_r, \delta\theta, \delta B_a, \delta S_a, \delta B_g, \delta S_g \right]^T \qquad (17)$$

where θ is the attitude vector; the other symbols are the same as these in Eq. (8).

Usually, the navigation output from the INS mechanization are in the n frame. In order to assure the coordinate frame of state parameters is consistent with that of INS, the corrections of position and velocity expressed in Eqs. (16) and (17) would be transformed from e frame into n frame by

$$\begin{pmatrix} \delta p_r \\ \delta v_r \end{pmatrix} = \begin{pmatrix} C_1(\delta p_{INS}^n + (C_b^n \iota^b \times)\delta\theta) \\ C_2\delta p_{INS}^n + C_n^e\big(\delta v_{INS}^n - \big((\omega_{en}^n \times + \omega_{ie}^n \times)C_b^n(\iota^b\times) + C_b^n(\iota^b \times \omega_{ib}^b)\times\big)\delta\theta + C_b^n(\iota^b\times)\delta\omega_{ib}^b\big) \end{pmatrix} \qquad (18)$$

where $p_{INS}^n = (B, L, h)^T$ and $v_{INS}^n = (v_N, v_E, v_D)^T$ are the geodetic coordinates and velocities in the n frame; ω_{en}^n and ω_{ie}^n denote the rotation rates of e frame with respect to the n frame, and the i frame with respect to the e frame, both projected in the n frame; $\delta\omega_{ib}^b$ is the gyroscope error vector including the biases and scale factor errors; the rotation matrix C_1 and C_2 can be expressed as

$$C_1 = \begin{bmatrix} -(R_N+h)\sin(B)\cos(L)/(R_M+h) & -\sin(L) & -\cos(B)\cos(L) \\ -(R_N+h)\sin(B)\sin(L)/(R_M+h) & \cos(L) & -\cos(B)\sin(L) \\ (R_N(1-e_0^2)+h)\cos(B)/(R_M+h) & 0 & \sin(B) \end{bmatrix} \qquad (19)$$

$$C_2 = \begin{bmatrix} \frac{-\cos(B)\cos(L)v_N+\sin(B)\cos(L)v_D}{(R_M+h)} & \frac{\sin(B)\sin(L)v_N+\cos(B)\sin(L)v_D}{(R_N+h)} & 0 \\ \frac{-\cos(B)\sin(L)v_N+\sin(B)\sin(L)v_D}{(R_M+h)} & \frac{-\sin(B)\cos(L)v_N-\cos(B)\cos(L)v_D}{(R_N+h)\cos(B)} & 0 \\ \frac{-\sin(B)v_N-\cos(B)v_D}{(R_M+h)} & 0 & -\sin(B) \end{bmatrix} \qquad (20)$$

where R_M and R_N denote the meridian radius and the prime circle radius respectively; e_0 is the ellipsoid eccentricity.

To describe the dynamic behavior of each parameter accurately, the classic state models (Shin, 2006; Brown and Hwang, 1997) are employed. Generally, the PSI angle error model is utilized to show the dynamic changes of position, velocity, and attitude, which can be defined as

$$\begin{pmatrix} \delta p_{INS,k}^n \\ \delta v_{INS,k}^n \\ \delta\theta_k \end{pmatrix} = \begin{pmatrix} (I - (\omega_{en}^n\times)\Delta t)\delta p_{INS,k-1}^n + \delta v_{INS}^n\Delta t \\ \chi\delta p_{INS,k-1}^n\Delta t + (I - ((2\omega_{ie}^n + \omega_{en}^n)\Delta t)\times)\delta v_{INS,k-1}^n \\ +(f^n\times)\Delta t\delta\theta_{k-1} + C_b^n\delta f^b\Delta t \\ (I - (\omega_{in}^n\times)\Delta t)\delta\theta_{k-1} - C_b^n\delta\omega_{ib}^b\Delta t \end{pmatrix} \qquad (21)$$

and the first order Gauss-Markov process (Brown and Hwang, 1997) is used to depict the time varying characters of IMU sensor errors

$$\begin{pmatrix} \delta B_k \\ \delta S_k \end{pmatrix} = \exp(-\Delta t/\tau)\begin{pmatrix} \delta B_{k-1} \\ \delta S_{k-1} \end{pmatrix} + \begin{pmatrix} v_B \\ v_S \end{pmatrix} \qquad (22)$$

and the random walk process (Brown and Hwang, 1997) is adopted to represent the dynamic behavior of the receiver clock offset and drift, the receiver hardware time delays, the residual of the zenith total delay of troposphere, and the ionospheric delays

$$x_k = x_{k-1} + v_x \qquad (23)$$

and the random constant model (Brown and Hwang, 1997) is employed to describe the changes of ambiguity

$$x_k = x_{k-1} \qquad (24)$$

where $\chi = \mathrm{diag}(\mathrm{g}/(R_M+h), \mathrm{g}/(R_N+h), 2\mathrm{g}/((R_MR_N)^{0.5}+h))$, g is the gravity; δf^b represents the accelerometer errors including biases and scale factor errors; the other symbols are the same as these introduced above.

Table 1
Performance parameters of POS810, POS1100, SPAN-FSAS, and MTi-G IMU sensors.

IMU sensors	Grade	Interval (Hz)	Gyroscopes			Accelerometers		
			Bias instability (°/h)	White noise (°/√h)	Scale factor (PPM)	Bias instability (mGal)	White noise (m/s/√h)	Scale factor (PPM)
POS810	Navigation	200	0.005	0.0022	10	25	0.00075	10
SPAN-FSAS	Tactical	200	0.75	0.1	300	1000	0.03	300
POS1100	Auto	200	10	0.33	1000	1500	0.18	1000
MTi-G	MEMS	100	216	3	3000	2000	0.12	3000

According to Eqs. (21)–(24), the state transition matrix in Eq. (15) can be achieved finally. Then, by applying the Kalman filter (Brown and Hwang, 1997), the parameters vector of the LCI mode and the TCI mode can be estimated.

2.4. INS update methodology

In the GNSS/INS integration system, the INS update phase works all the time to provide continuous navigation solutions with higher sample rate no matter there is GNSS data or not. Generally, the procedure is implemented by the INS mechanization based on the following navigation functions (Savage, 2000; Shin, 2006)

$$\begin{pmatrix} \dot{\boldsymbol{v}}_{INS}^n \\ \dot{\boldsymbol{p}}_{INS}^n \\ \dot{\boldsymbol{C}}_b^n \end{pmatrix} = \begin{pmatrix} \boldsymbol{C}_b^n \boldsymbol{f}^b - (2\boldsymbol{\omega}_{ie}^n + \boldsymbol{\omega}_{en}^n) \times \boldsymbol{v}_{INS}^n + \boldsymbol{g}^n \\ \boldsymbol{v}_{INS}^n \\ \boldsymbol{C}_b^n (\boldsymbol{\omega}_{ib}^b \times) - ((\boldsymbol{\omega}_{ie}^n + \boldsymbol{\omega}_{en}^n) \times) \boldsymbol{C}_b^n \end{pmatrix} \quad (25)$$

In detail, the velocity update discrete expression can be written as follows (Shin, 2006)

$$\boldsymbol{v}_k^n = \boldsymbol{v}_{k-1}^n + 0.5[\boldsymbol{C}_{n(k-1)}^{n(k)} + \boldsymbol{I}]\boldsymbol{C}_{b(k-1)}^{n(k-1)}\Delta\boldsymbol{v}_{f(k)}^{b(k-1)}$$
$$+ \Delta t[\boldsymbol{g}^n - (2\boldsymbol{\omega}_{ie}^n + \boldsymbol{\omega}_{en}^n) \times \boldsymbol{v}^n]_{mid} \quad (26)$$

where $\boldsymbol{C}_{n(k)}^{n(k-1)}$ is the rotation matrix of n frame from epoch $k-1$ to k; $\boldsymbol{v}_{f(k)}^{b(k-1)}$ denotes the velocity increments at epoch k with respect to epoch $k-1$ calculated by making integral on specific force after the compensation of the rotation and sculling effects; the subscript *mid* refers to the middle time between $k-1$ and k time; the other parameters are the same as mentioned above. The position update is divided into two phases, where the vertical component can be expressed as

$$h_k = h_{k-1} - v_{D,mid}\Delta t \quad (27)$$

and the horizontal position components are updated by (Shin, 2006)

$$\boldsymbol{q}_{n(k)}^{e(k)} = \begin{pmatrix} \cos(\|0.5\zeta_k\|) \\ -\sin(\|0.5\zeta_k\|)0.5\zeta_k/\|0.5\zeta_k\| \end{pmatrix} \otimes \boldsymbol{q}_{n(k-1)}^{e(k-1)}$$
$$\otimes \begin{pmatrix} \cos(\|0.5\xi_k\|) \\ \sin(\|0.5\xi_k\|)0.5\xi_k/\|0.5\xi_k\| \end{pmatrix} \quad (28)$$

where $\boldsymbol{q}_{n(k)}^{e(k)}$ and $\boldsymbol{q}_{n(k-1)}^{e(k-1)}$ represent the position quaternion at epoch $k-1$ and k respectively; $\xi_k = \boldsymbol{\omega}_{ie}^n \Delta t$ and $\zeta_k = (\boldsymbol{\omega}_{in}^n)_{mid}\Delta t$ stand for the angle variation of e frame and n frame with respect to the i frame projected in the n frame; $\otimes$ denotes the quaternion multiplication. Then, according to the relationship between position quaternion and geodetic coordinate, the latitude and longitude can be obtained. The attitude update can be defined as following expression (Savage, 2000; Shin, 2006)

$$\boldsymbol{q}_{b(k)}^{n(k)} = \begin{pmatrix} \cos(\|0.5\zeta_k\|) \\ -\sin(\|0.5\zeta_k\|)0.5\zeta_k/\|0.5\zeta_k\| \end{pmatrix} \otimes \boldsymbol{q}_{b(k-1)}^{n(k-1)}$$
$$\otimes \begin{pmatrix} \cos(\|0.5\varsigma_k\|) \\ \sin(\|0.5\varsigma_k\|)0.5\varsigma_k/\|0.5\varsigma_k\| \end{pmatrix} \quad (29)$$

where ς_k is the attitude increment computed by using the angular rate after the coning effect correction. Then, the attitude quaternion could be transformed to the Euler angles (*i.e.*, roll, pitch, and heading) (Shin, 2006).

3. Implementation, test, and results

This section illustrates the implementation, tests, and discussions. The implementation is first provided, followed by the test description and the results including the positioning performance of the BDS/GPS PPP and the PPP/INS integration, the attitude determination performance of the BDS/GPS PPP/INS integration, the BDS + GPS PPP/INS integration under the complete GNSS outage situations, and the positioning performance of the BDS + GPS PPP/MEMS INS TCI mode under the partial GNSS outage situations.

Fig. 1 shows the implementation of the mathematical models introduced above, mainly including the INS navigation part, the GNSS raw PPP, the PPP/INS loosely coupled integration, and the PPP/INS tightly coupled integration. Generally, the measurements from IMU sensor will be compensated before it can be applied in INS mechanization for the update of position, velocity, and attitude. Then, the Kalman time update phase would be operated to achieve the covariance of the solutions. After that, a synchronization between INS and GNSS is necessary based on the Pulse Per Second number (PPS) of the IMU outputs and the GNSS observing time, which is to check whether there are GNSS solutions and/or GNSS observations. When they are synchronized, the GNSS raw PPP/INS integration model would work. If using the GNSS solutions (position and velocity), the loosely coupled integration model is going to operate, otherwise, the tightly coupled integration model is working. Finally, the parameters estimated by Kalman filter will be utilized to correct the INS solutions and to compensate the IMU sensor errors by a closed loop feedback process.

3.1. Land-borne experiment and data processing schemes

In order to assess the performance of the BDS + GPS PPP/INS TCI mode and the influence of IMU grades on the performance of the PPP/INS integration, a set of land-borne vehicle BDS + GPS + INS data is collected around Wuhan, China (the trajectory is shown in Fig. 2 (a)). The motions in detail of the test are shown in Fig. 3 in terms of the time varying of the velocity (±20 m/s) and attitude. In this test, four different grade IMUs, namely POS810 (navigation grade) and POS1100 (auto grade) from Wuhan MaiPu space time company

(http://www.whmpst.com/en/page.php?cid=13), SPAN-FSAS (tactical grade) from NovAtel company (http://www.novatel.com/products), and MTi-G (MEMS grade) from Xsens company (https://www.xsens.com/products/) are equipped together with a BDS + GPS receiver (Trimble NetR9). The basic information about these IMU sensors are listed in Table 1.

The BDS/GPS observations and the data from four IMUs are processed in PPP mode, PPP/INS LCI mode, and PPP/INS TCI mode using the forward Kalman filter. To weaken the impacts of satellite orbit and clock errors on positioning performance, the precise satellite orbit and clock products of BDS and GPS provided by Wuhan University are utilized. Such precise products are calculated using the BDS/GPS data from the International GNSS Monitoring and Assessment Service (IGMAS) network. Currently, the IGMAS network includes 15 tracking stations with 12 stations in Asia, 2 stations in Europe, and 1 station in Antarctica (the red-blue circles in the left subfigure of Fig. 2). The sky plots of the observed BDS (B) and GPS (G) satellites in this test are displayed in Fig. 2(a). The current BDS satellite constellation consists of Geostationary Earth Orbit (GEO) satellites and inclined Geo-Synchronous Orbit (IGSO) satellites; therefore, the continuity of BDS observation is better than that of GPS in the test area.. The corresponding available satellite numbers and Position Dilution of Precision (PDOP) of BDS and GPS are depicted in Fig. 2(b). The number of available satellites decreases frequently when the satellites with lower elevation angles are blocked by unexpected observing conditions. According to the statistics, the average satellite numbers of BDS, GPS, and BDS + GPS during the whole mission are 6.2, 8.6, and 14.8, and the corresponding average PDOP are 5.6, 2.1, and 1.7, respectively. Obviously, the BDS + GPS can provide more available satellites and better spatial geometry structure for users. Besides, due to the GEO satellites almost keep static over the equator which makes the spatial geometry structure of BDS worse than that of GPS, we can see from Fig. 2(b) that the PDOP of BDS is affected visibly by the motions of IGSO satellites. Such phenomenon does not occur while using GPS data.

In order to evaluate the performance of the BDS/GPS PPP and the PPP/INS integration mode, the smoothing solutions of position and attitude calculated by the BDS + GPS RTK/POS810 LCI mode are adopted as the reference values. Then, the position differences between our solutions and the reference values are transformed to the navigation frame (North, East, and Down), and the attitude will be analyzed in terms of roll, pitch, and heading angles. Meanwhile, five 60-second complete and partial BDS + GPS outages with each separated by 1000 seconds (shown in Fig. 3) are generated to evaluate the impacts of INS grade on the performance of the BDS + GPS PPP/INS TCI mode and LCI mode under the situations when the receiver loses all or part of the satellite signals due to the unexpected environmental conditions such as tunnels, tree shades, and overpasses.
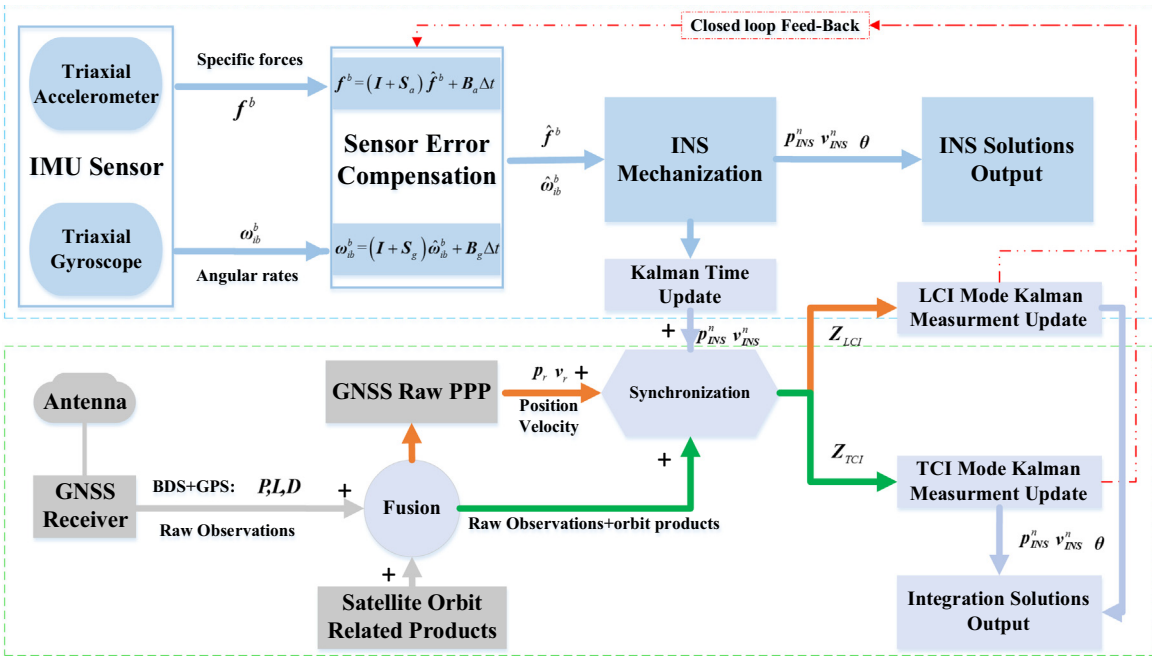
Fig. 1. Implementation of BDS/GPS raw observations based PPP, PPP/INS loosely coupled integration, and PPP/INS tightly coupled integration.
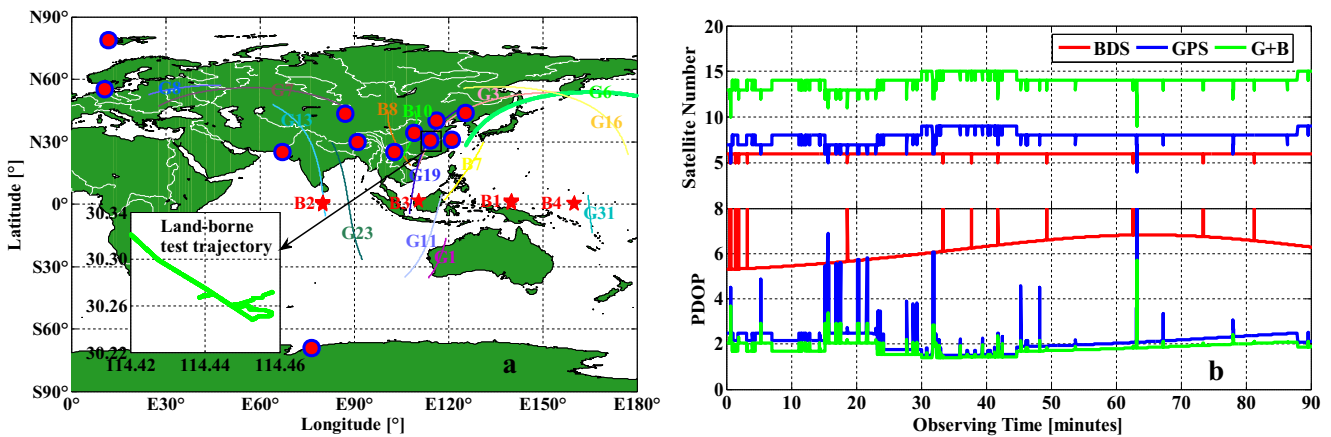

Fig. 2. Sub-figure (a) shows satellite sky plots of BDS (B) and GPS (G), IGMAS stations, and the trajectory of the land-borne experiment; sub-figure (b) shows available satellites number of BDS, GPS, and GPS + BDS (G + B), and the corresponding PDOP.

3.2. Positioning performance of BDS/GPS PPP and PPP/INS integration

Shown in Fig. 4 are the position differences between the results calculated based on the two strategies (the raw PPP and the PPP/INS LCI) using three types GNSS data (BDS, GPS, and GPS + BDS) and four grades IMU measurements (POS810, SPAN-FSAS, POS1100, and MTi-G). Significantly, as is proved by the previous studies (Odijk et al., 2015; Pan et al., 2015; Chen et al., 2016), with the help of BDS, the positioning accuracy of PPP can be enhanced significantly, which can be found from Fig. 4(a). Especially, there are noticeable jumps, which are caused by the insufficient satellite observations and the poor PDOP, in the position results from both the BDS PPP and the GPS

PPP around 62 min. These jumps disappeared in the BDS + GPS PPP mode, in which more available satellites and better PDOP are obtained. Besides, the stability of the BDS + GPS PPP is also much better than that of BDS PPP and GPS PPP. According to the statistics of the results in Fig. 5(d), the Root Mean Square (RMS) values of the kinematic PPP in north, east, and vertical components are improved from 15.3, 13.3, and 29.5 cm of the BDS PPP and 10.5, 19.3, and 28.0 cm of the GPS PPP to 6.2, 11.8, and 21.5 cm while using the BDS and GPS together. The average improvements in the three position directions are approximately 50.2, 24.9, and 25.0%, respectively. The position accuracy of the BDS PPP is better than that of the GPS PPP in the east-west direction due to the special satellite constellation structure of BDS. For BDS,
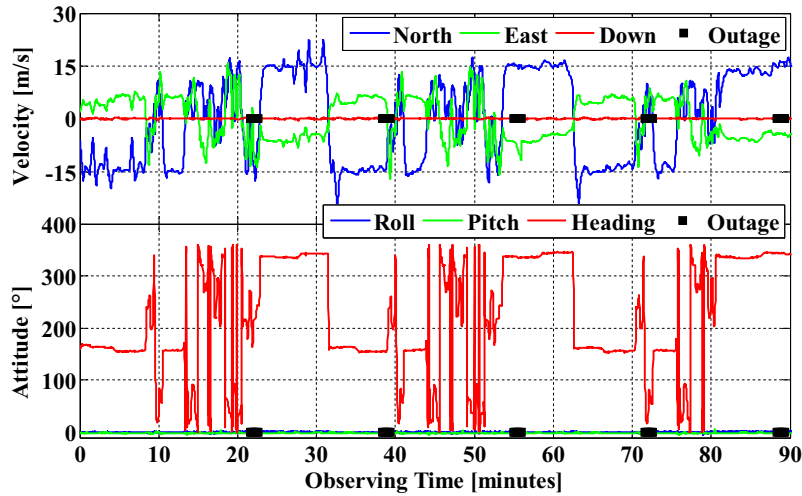
Fig. 3. Velocity (top) and attitude (bottom) changed along with time; the black panes show the time-period when the GNSS outage simulations happened.
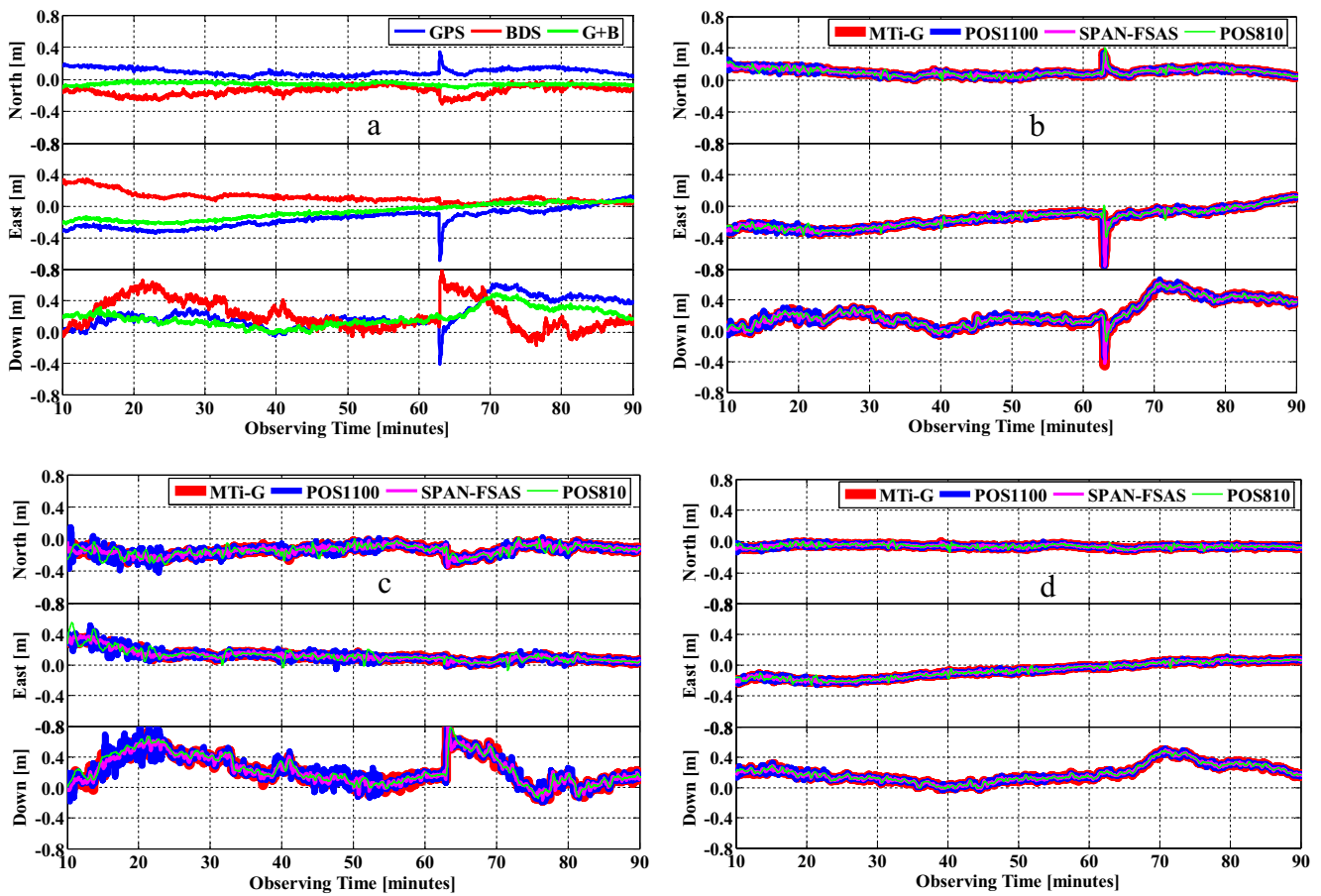

Fig. 4. Position differences of the PPP mode (a), the GPS PPP/INS LCI mode (b), the BDS PPP/INS LCI mode (c), and the BDS + GPS PPP/INS LCI mode (d) compared to the reference values; in the LCI mode, all the four different grade IMU data are processed.

the GEOs are over the equator distributing along the east-west direction (seen in the left subfigure of Fig. 2), which makes the geometry structure of positioning in this direction much stronger than the other two directions and leads to a better position results.

The results depicted in the Fig. 4(b), (c), and (d) are computed in the PPP/INS LCI mode using the PPP solutions of GPS, BDS, and BDS + GPS and the IMU data from POS810, SPAN-FSAS, POS1100, and MTi-G. According to the results listed in Fig. 4(d), the position
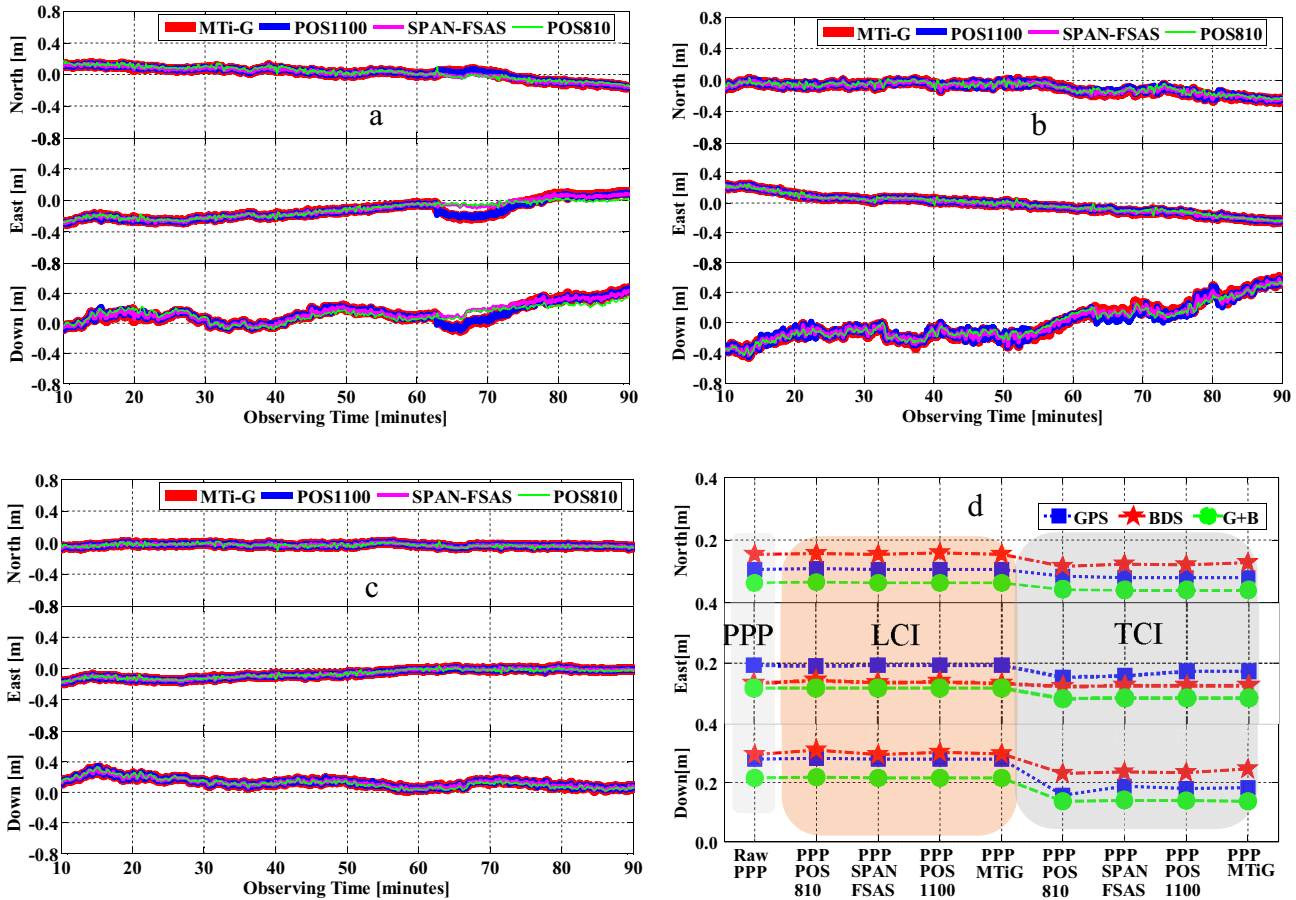
Fig. 5. Position differences of the GPS PPP/INS TCI (a), the BDS PPP/INS TCI (b), the BDS + GPS PPP/INS TCI (c), and the position RMS (d) of all the data processing methods compared to the reference values.

RMS differences among the PPP/INS LCI solutions that use four different grade IMUs are less than 0.5 cm. This outcome appears no matter whether GPS PPP, BDS PPP, or BDS + GPS PPP is used. The average position RMS values are 15.4, 13.4, and 29.7 cm in north, east, and vertical for the BDS PPP/INS LCI mode, 10.5, 19.1, and 28.0 cm for the GPS PPP/INS LCI mode, and 6.2, 11.8, and 21.6 cm for the BDS + GPS PPP/INS LCI mode. Clearly, the position accuracy of the PPP/INS LCI mode is almost the same as that of PPP when using the same GNSS observations. The reason for this outcome is that in the PPP/INS LCI mode, the INS data has no contribution on PPP calculation. Therefore, the positioning accuracy of LCI mode depends mainly on the accuracy of PPP when there are enough satellite observations for PPP calculation, which is presented clearly in Fig. 4(d). Otherwise, if there are not enough satellite observations for PPP computation, PPP cannot output positioning results, and the PPP/INS LCI mode will provide the navigation results by processing the IMU data only in the INS mechanization (as shown in Fig. 1). During the partial or complete GNSS outage periods, the performance of PPP/INS LCI will be determined by the performance of IMU sensors. It can be proved visibly by Fig. 4(b) and (c), in which the position drifts of the

PPP/POS810 LCI mode at about 62 min is smaller than the solutions when other IMUs are used.

Different from the PPP/INS LCI mode, the PPP/INS TCI mode is based on the satellite raw observations and IMU predicted GNSS values, which makes it possible that the INS data can contribute to the parameter estimation of PPP because of the strong correlation among the INS related errors and the PPP related parameters such as the float ambiguities, zenith tropospheric delay, and ionospheric delay. Thus, by comparing Fig. 5 with Fig. 4, the results of the PPP/INS TCI mode are more accurate than those from the PPP mode and the PPP/INS LCI mode even when adopting the same GNSS observations. According to the RMS statistics of Fig. 5(d), the average position RMS of the BDS PPP/INS TCI mode are 12.1, 12.5, and 23.6 cm in north, east and vertical, with improvements of 21.3, 6.2, and 19.8% compared to the PPP/INS LCI mode. Similarly, compared to LCI mode, there are position accuracy improvements of approximately 24.4, 15.0, and 36.8% when using the GPS PPP/INS TCI mode (mean RMS: 7.9, 16.4, and 17.7 cm), and nearly 37.4, 27.5, and 36.1% enhancements while using the BDS + GPS PPP/INS TCI mode (average RMS: 3.9, 8.5, and 13.7 cm). To achieve the influence of IMU grade on GNSS/INS integration,

we analyzed the solutions in TCI mode using the same GNSS data and different IMU measurements. The largest position RMS differences among the four BDS data based PPP/INS TCI modes are 1.0, 0.2, and 1.5 cm in north, east, and vertical direction. Similarly, such differences are 0.5, 2.0, and 3.0 cm for the GPS based PPP/INS TCI mode, and 0.2, 0.2, and 0.1 cm for the BDS + GPS based PPP/INS TCI mode. Obviously, using more GNSS systems' data can reduce the positioning dependency of the PPP/INS integration system on the INS grade, when either LCI or TCI is used.. Although the PPP/INS TCI mode can work as long as there are GNSS observations, the positioning performance is highly depended on the performance of IMU sensor when there are not enough GNSS observations. It is also why the GNSS partial outage related position jumps in PPP and PPP/INS LCI in Fig. 5(a) around 62 min only can be mitigated partly in the PPP/INS TCI mode. Therefore, when there are not enough GNSS observations, the position RMS differences among the different IMU based PPP/INS TCI modes become larger.

3.3. Attitude determination performance of BDS/GPS PPP/INS integration

Besides the aid in positioning, with help of INS angular rate measurements, PPP/INS integration is also a practical technology to provide attitude. Different from the dual-antenna GNSS attitude determination algorithm, user can conveniently obtain the attitude information by integrating a GNSS receiver and an IMU. After the attitude initial alignment (Shin, 2006), the attitude corrections can be estimated precisely in Kalman filter because of the relationship between the attitude errors and the GNSS information (i.e., GNSS positioning results: position and velocity, or GNSS raw observations: pseudo-range, carrier-phase, and Doppler) as shown in Eqs. (18) and (21).

Fig. 6 shows the attitude differences between the reference values and the solutions computed in the PPP/INS LCI mode and the PPP/INS TCI mode using the four IMUs. Here, the subfigures (a), (c), and (e) are calculated in the PPP/INS LCI mode with the PPP solutions based on GPS, BDS, and BDS + GPS. Subfigures (b), (d), and (f) are processed in the PPP/INS TCI mode using the raw observations of GPS, BDS, and BDS + GPS, respectively. All subfigures in Fig. 6 illustrate that:

(1) The accuracy of attitude determination in both the PPP/INS LCI and TCI modes is highly depended on the grade of IMU sensors. According to the statistics in Fig. 7, the PPP/POS810 integration (LCI mode and TCI mode) can provide the best attitude solutions (with RMS values of 0.001, 0.001, and 0.011° in roll, pitch, and heading directions, respectively). The PPP/SPAN-FSAS integration results are about 10 times larger (with RMS values of 0.111, 0.073, and 0.104°) than that of the PPP/POS810. Further-

more, PPP/POS1100 integration results RMS are 0.216, 0.165, and 0.337°, which are about 2–4 times larger than those of PPP/SPAN-FSAS integration. Finally, the attitude errors of the PPP/MTi-G integration are the worst, with the RMS values of 0.191, 0.194, and 0.835°.

(2) There is strong relationship between IMU sensor grade and the stability of attitude solutions. In general, it is because that higher grade IMU sensors have better measuring sensitivity on the motion of platform in body frame which can provide velocity increments and angle increments with smaller errors and noises.

(3) The attitude RMS differences between the PPP/INS LCI mode and the PPP/INS TCI mode are very small with maximum value of ±0.002°, ±0.015°, ±0.026°, and ±0.022° for POS810, SPAN-FSAS, POS1100, and MTi-G based PPP/INS integration, respectively. This phenomenon indicates that the choice of GNSS updates (using either position and velocity, or pseudo-range, carrier-phase, and Doppler) does not have significant impact on the PPP/INS attitude determination. This outcome is different from that of positioning.

Besides, the attitude accuracy in the heading direction is lower than the other two components. Generally, it is owing to the weak observability of the heading when the vehicle is moving straight with a relatively stable speed. The observability of heading can be enhanced by either adding extra sensors such as magnetometers, or introducing vehicle dynamics such as accelerating and turning.

3.4. BDS+GPS PPP/INS integration working in complete GNSS outage situations

To evaluate the performance of the PPP/INS integration (LCI and TCI) in the unexpected conditions (e.g., GNSS outages), we add five 60-second complete satellite signal outages with each one separated by 1000 seconds to the BDS + GPS raw observations as shown in Figs. 2 and 8 (a). These simulated GNSS data are re-processed together with the four IMU, and in LCI and TCI modes, respectively.

We evaluate the performance of the TCI mode in two cases. First, we use the data that have excluded the outage periods to investigate the performance of recovery after GNSS outages (e.g., by evaluating the convergence speed and positioning accuracy). This procedure is important because short-term GNSS outages are common for land vehicles which is the major fact limiting the application of PPP in the dynamic applications. Second, only the outage data are processed to evaluate the performance of INS during the outage periods. To study the performance of recovery after GNSS outages, Fig. 8(a) and (b) illustrate the position results of processing the data without the GNSS outage periods by using the BDS + GPS PPP/INS
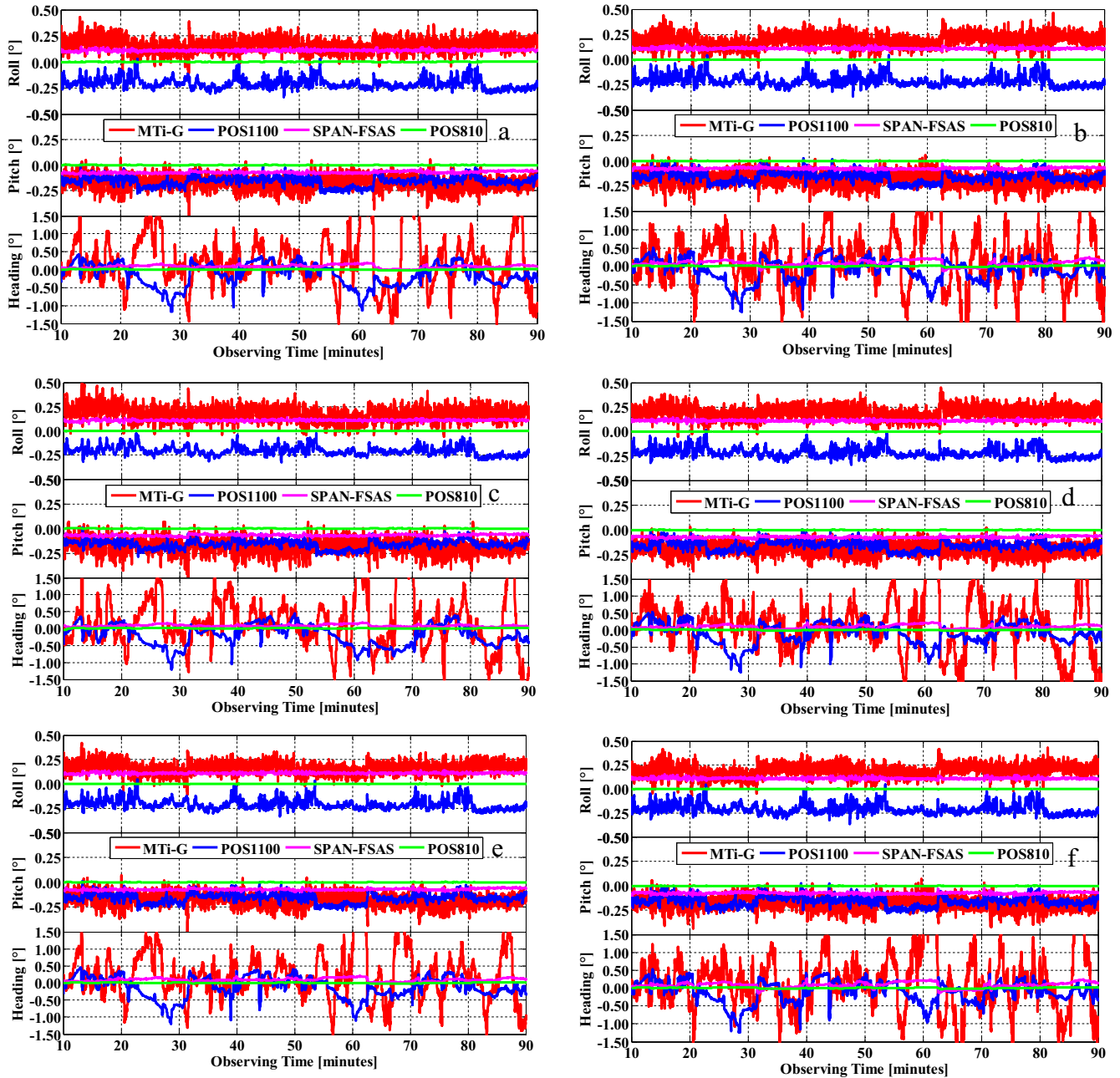
Fig. 6. Attitude differences time series calculated between the reference attitude values and the solutions from the PPP/INS LCI mode and the PPP/INS TCI mode using GPS, BDS, and BDS + GPS observations and the IMU data collected from POS810, SPAN-FSAS, POS1100, and MTi-G sensors in the same test; subfigures (a), (c), and (e) are the attitude solutions from the PPP/INS LCI mode using GPS, BDS, and BDS + GPS data; subfigures (b), (d), and (f) are the attitude solutions from the PPP/INS TCI mode using GPS, BDS, and BDS + GPS data.

LCI and TCI modes. After the evaluation, we can know that:

(1) The PPP/INS TCI mode expressed a better performance than the PPP/INS LCI mode in terms of both convergence speed and positioning accuracy, especially in the east and vertical components. The main reason for this outcome is the strong correlations between INS related parameters and GNSS float ambiguities and atmosphere related parameters in

the PPP/INS TCI mode. Such correlations will bring strong constraints in the parameter estimation in the PPP/INS TCI mode when the GNSS signals are locked again. According to the corresponding statistical results, the average position RMS of the PPP/INS TCI mode are 18.6, 13.8, and 29.2 cm in north, east, and down directions, respectively, which provides improvements of 1.9, 87.1, and 63.2% when compared to 19.0, 25.8, and 47.7 cm of the PPP/INS LCI mode.
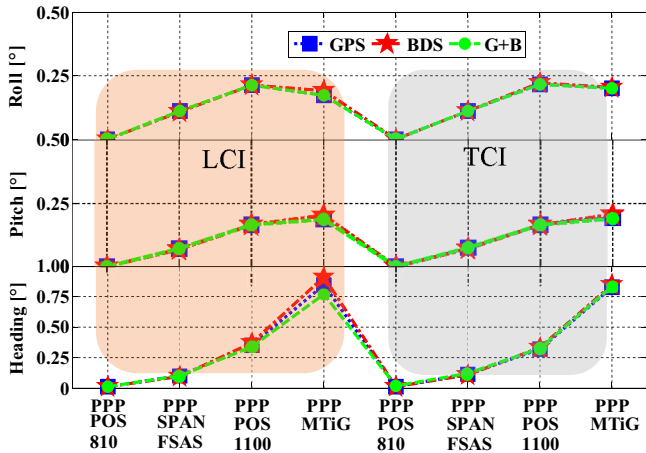
Fig. 7. RMS of attitude calculated in the PPP/INS LCI mode (left-hand slot) and the PPP/INS TCI mode (right-hand slot) using GPS, BDS, and BDS + GPS observations and the IMU data collected from POS810, SPAN-FSAS, POS1100, and MTi-G sensors in the same test.

(2) For the impact of different IMUs, the position differences among the four IMU based PPP/INS LCI schemes are not remarkable with the maximum values of 3.1, 1.1, and 2.8 cm in the three position components. Such differences in the PPP/INS TCI mode are up to 13.6, 5.0, and 16.4 cm which are very notable. Also, about 9.4, 10.7, and 19.3 cm can be obtained while using the POS810 IMU data in the BDS + GPS PPP/INS TCI mode, which is much more accurate than the other three PPP/INS TCI schemes and all of the four PPP/INS LCI shames. It may due to the fact that higher grade IMU can provide more accurate predicted positions and tighter constraint in the PPP/INS TCI mode. Comparing the solutions in Fig. 5(c) with these in Fig. 8(b), about 58.3, 20.8, and 29.1% position accuracy are lost in the BDS + GPS PPP/POS810 TCI mode.

Fig. 9 shows the attitude solutions from the BDS + GPS PPP/INS LCI and TCI modes by processing the GNSS outage simulation data. Different from the position solutions, there only less than 8.6% attitude accuracy are lost in both the PPP/INS LCI mode and the PPP/INS TCI mode compared to the solutions in Fig. 6(f). Such outcome indicates that the impact of the 60-second GNSS outages on the attitude determination is not significant, especially while using higher grade IMU sensors. Generally, it is because (1) the attitude drifts during the GNSS outage periods has not exceeded the attitude determination accuracy of INS; (2) the attitude drifts can almost be estimated accurately when the PPP/INS integration works after the GNSS outages.

During the complete GNSS outage periods, no GNSS solutions or GNSS raw observations can be utilized. Thus, both the PPP/INS LCI and TCI modes cannot work. In the case, only the INS mechanization (Savage, 2000; Shin, 2006) works by processing the IMU data. Shown in Figs. 10 and 11 are the results of position and attitude calculated by the INS mechanization during the complete GNSS outage periods using the four types IMU data. Significantly, both position and attitude solutions diverge along with the increasing GNSS outage time. Such divergent speed is visibly depended on the grade of IMU sensors. Generally, the POS810 can provide better solutions than the other three IMUs, and the results from MTi-G are the lowest. However, when the GNSS outage time is less than 10 s, INS can also provide users decimeter level positioning results (as depicted in Fig. 10) even while using the MEMS IMU (MTi-G). According to the corresponding statistics, the position accuracies computed by POS810 drops from 0.4, 0.1, and 0.2 cm to 27.3, 43.9, and 16.6 cm in north, east, and down components along with GNSS outage time increasing from 1 s to 60 s. Such results are about 10 times more accurate than that of SPAN-FSAS (the maximum values are 353.0, 440.3, and 26.9 cm), 20 times more accurate than these of POS1100 (the maximum values are 544.3, 597.8, and 801.3 cm), and about 200 times better than these of MTi-G (the maximum values are 2549.1, 8086.3, and 536.3 cm). Similarly, the maximum of
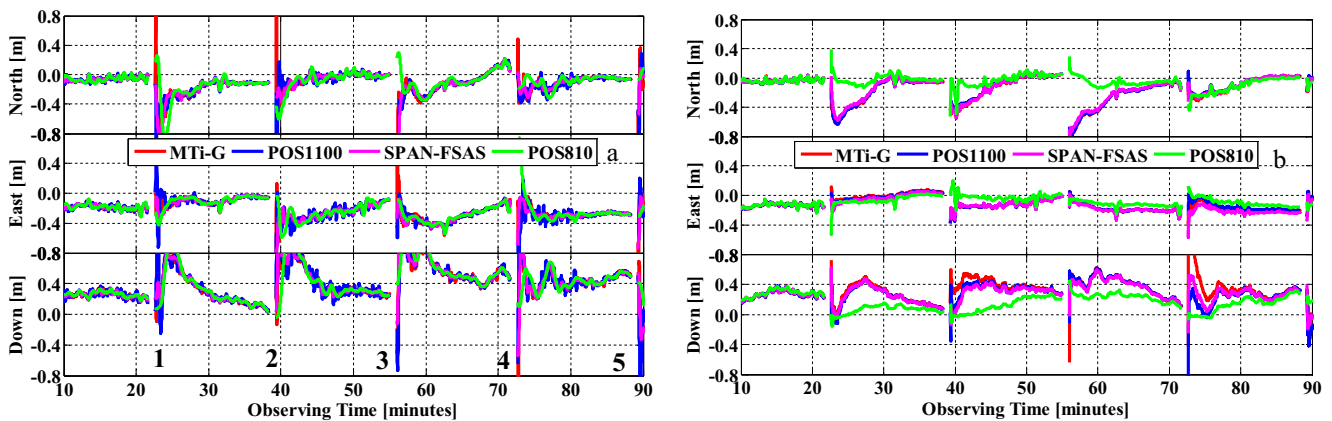

Fig. 8. In the 60-second satellite signal outage simulation scenes, the position differences time series of the PPP/INS LCI mode (a) and the PPP/INS TCI mode (b) using the BDS + GPS observations, POS810, SPAN-FSAS, POS1100, and MTi-G IMU data.
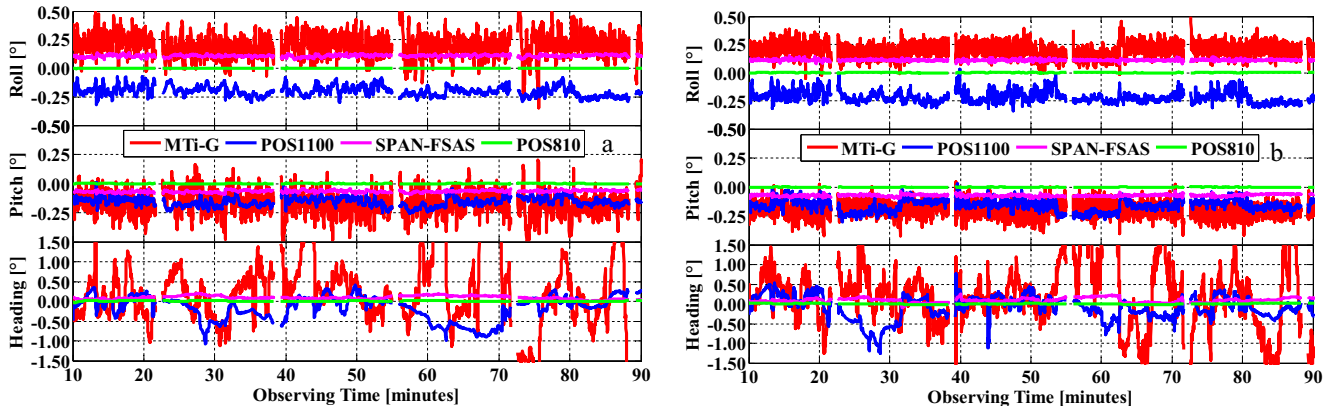
Fig. 9. In the 60-second satellite signal outage simulation scenes, the attitude differences time series of the PPP/INS LCI mode (a) and the PPP/INS TCI mode (b) using the BDS + GPS observations, POS810, SPAN-FSAS, POS1100, and MTi-G IMU data.
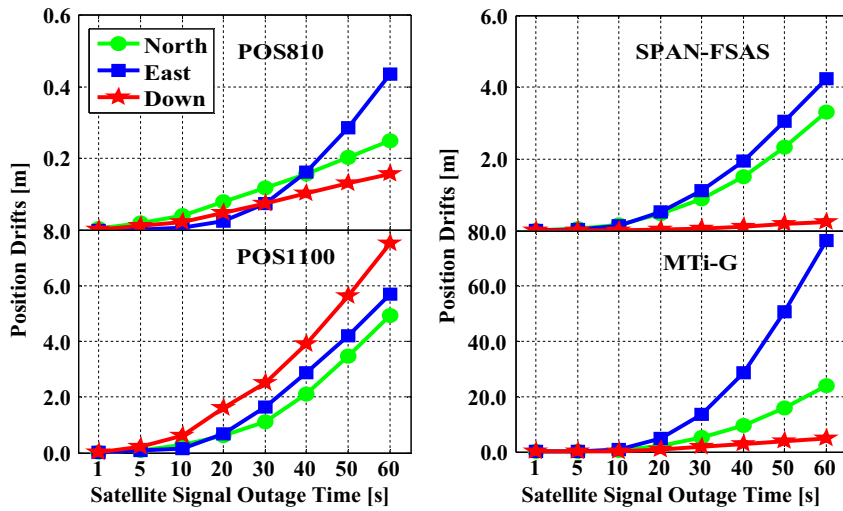

Fig. 10. During the 60-second satellite signal outage simulation scenes, the position drifts calculated by the INS mechanization using POS810, SPAN-FSAS, POS1100, and MTi-G data.
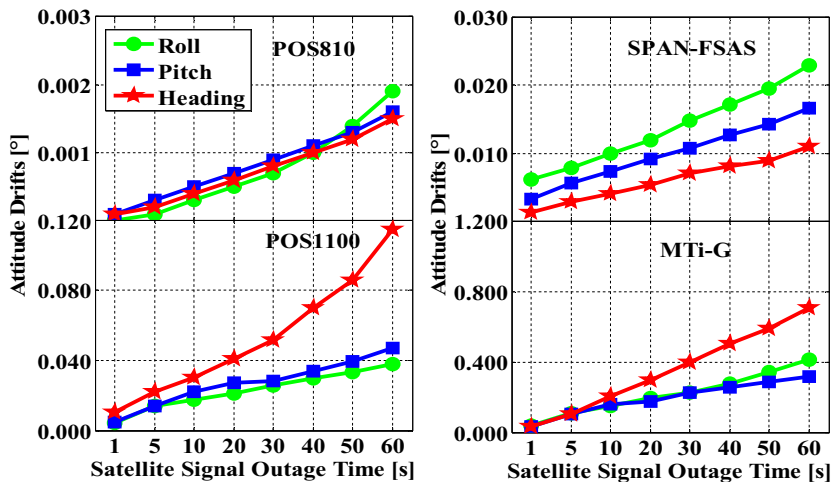

Fig. 11. During the 60-second satellite signal outage simulation scenes, the attitude drifts calculated by the INS mechanization using POS810, SPAN-FSAS, POS1100, and MTi-G data.
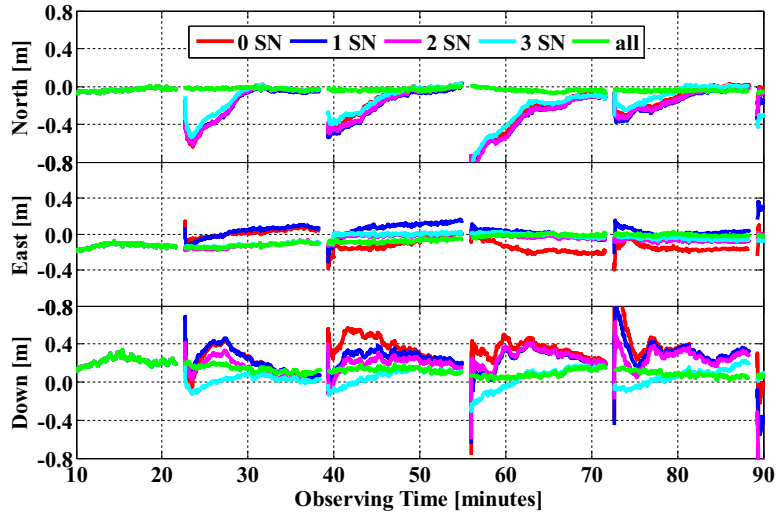
Fig. 12. Position differences time series of the BDS + GPS PPP/MTi-G tightly coupled integration in the 60-second partial GNSS outage simulations; here "X SN" means X available Satellite Numbers (SN), "all" presents the solutions without GNSS outage simulation.
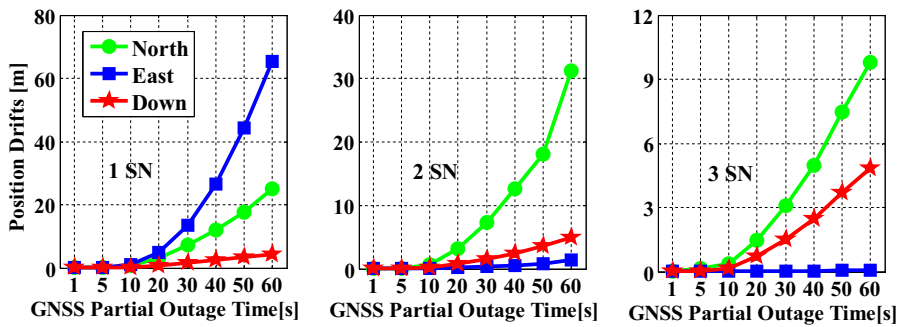

Fig. 13. Position drifts of the BDS + GPS PPP/MTi-G tightly coupled integration during the 60-second partial GNSS outage periods; here "X SN" means X available Satellite Numbers (SN).

attitude drift of POS810 is 0.002° during the 60-second GNSS outages, which presents about 10 times, 10–20 times, and 100–200 times more accurate than these of calculated from SPAN-FSAS, POS1100, and MTi-G, respectively. It is mainly caused by the different time-varying IMU sensor errors, which will impact on the accuracy of INS mechanization due to the reason as described by Eqs. (13) and (14) during the complete GNSS outage periods.

3.5. Positioning performance of BDS+GPS PPP/MEMS INS TCI mode in partial GNSS outage situations

One of the most important advantages of PPP/INS TCI mode compared the LCI mode is that TCI mode can work under the partial GNSS outage situations. Such situations may happen in many dynamic applications. Therefore, the positioning performance of PPP/INS TCI mode in partial GNSS outage condition is furtherly evaluated by processing the BDS + GPS observations and MTi-G data with pre-set outage time periods (outage 60 s in every 1000 seconds). During each partial outage period, only 1, 2, and 3

available satellite number (SN) were used. Similar to the complete outage tests, we evaluate the performance of the TCI mode in two cases, specifically, (a) investigating the performance of recovery after the GNSS outages, and (b) evaluating the performance during the outage periods. The results of (a) are depicted in Fig. 12. It can be seen that more available satellites are helpful in improving the accuracy and re-convergence of the PPP/INS TCI positioning. Even one available satellite can be useful for the recovery of PPP in the TCI mode. Moreover, with the usage of available satellites during the partial GNSS outage periods, the PPP/INS TCI position divergence speed is also restrained significantly.

The PPP/INS TCI positioning results during partial outage periods are shown in Fig. 13. According to the statistical results, the maximum position drifts in north, east, and down components are reduced from 2549.1, 8086.3, and 536.3 cm to 976.8, 7.1, and 482.6 cm along with the available satellite number increasing from 0 to 3 during the GNSS outages. Compared to the position solutions without GNSS, more than 17.5, 62.8, and 87.2% three-dimensional position improvements can be obtained when

1 SN, 2 SNs, and 3 SNs are used, respectively. There are two reasons for this fact: first, the related IMU sensor errors can be estimated in the PPP/INS TCI mode during the partial outage periods; second, the observed GNSS data can be utilized to estimate the corrections for the Kalman filter states. Therefore, it is preferred to use the PPP/INS TCI mode in the unpredictable environments to obtain more accurate position solutions compared to the PPP mode and the PPP/INS LCI mode.

4. Conclusions

Based on the mathematic model of GNSS raw PPP and the methodology of INS navigation, the algorithm of the TCI mode between raw PPP and INS is investigated in this paper. In order to assess the performance of the PPP/INS TCI mode and to evaluate the impact of IMU grade on the PPP/INS TCI mode, a set of BDS + GPS observation and four different grade IMU data collected from a land-borne experiment are processed and analyzed. In addition, the complete and partial GNSS outages are generated to the original BDS + GPS observations to evaluate the performance of the PPP/INS TCI mode in the unexpected city canyon conditions. According to the experimental results, the positioning performance of the raw PPP/INS TCI mode in terms of accuracy and re-convergence are much more accurate than those from the raw PPP mode and the raw PPP/INS LCI mode in both the open sky conditions and the challenged environments, especially while using the BDS + GPS observations.

In general, the dynamic positioning accuracy of BDS PPP is almost the same as that of GPS PPP, even a little better in the east components. It is due to the special satellite-constellation of BDS in the test area, which consists of GEOs and IGSOs. Due to such satellite constellation, BDS can provide better observation in continuity and better positioning performance in the east direction. When BDS and GPS are combined in PPP mode, the positioning accuracy is enhanced visibly with about 50.2, 24.9, and 25.0% improvements. In the PPP/INS TCI mode, about 27.7, 16.2, and 30.9% average improvements can be got compared to the results from the PPP mode and the PPP/INS TCI mode. Especially, about 3.9, 8.5, and 13.7 cm positioning RMS can be achieved while using the BDS + GPS data. Besides, the results provided by the PPP/INS TCI mode are much more stable and continuous. Meanwhile, the positioning results of both the PPP/INS TCI mode and the PPP/INS LCI mode in open sky are highly depended on the number of the available GNSS observations and slightly determined by the grade of IMU sensors. However, a strong relationship between the position accuracy of the PPP/INS TCI and LCI modes and the IMU grade can be presented when the GNSS observability is poor. Differently, the attitude accuracy will always be mainly determined by the IMU grade.

According to the GNSS outage results, the accuracy of both position and attitude of the PPP/INS TCI mode

degrades dramatically along with the increasing outage time, especially for low grade IMUs. However, the available satellite signals during the partial GNSS outages can be helpful in restraining the divergence of position, even when there is only one available satellite. Generally, about 17.5, 62.8, and 87.2% three-dimensional position improvements can be obtained when there are 1, 2, and 3 available satellites, respectively. Besides, with more available satellites using during the partial GNSS outage periods (*i.e.*, satellite number from zero to three), the PPP/INS TCI mode position divergence speed is also restrained significantly. This outcome means that there is a large potential in improving the positioning performance compared to the widely used GNSS based positioning technology at present. Therefore, it is preferred to use the PPP/INS TCI mode in the unpredictable environments (*e.g.*, urban canyon) to obtain much more accurate position solutions compared to the PPP mode and the PPP/INS LCI mode.

References

Bertiger, W., Desai, S.D., Haines, B., Harvey, N., Moore, A.W., Owen, S., Weiss, J.P., 2010. Single receiver phase ambiguity resolution with GPS data. J. Geodesy 84 (5), 327–337.

Brown, R.G., Hwang, P.Y.C., 1997. Introduction to Random Signals and Applied Kalman Filtering. Willey, New York.

Chen, J., Wang, J., Zhang, Y., Yang, S., Chen, Q., Gong, X., 2016. Modeling and assessment of GPS/BDS combined precise point positioning. Sensors 16 (7), 1151. http://dx.doi.org/10.3390/s16071151.

Cox, D.B., 1978. Integration of GPS with inertial navigation systems. Navigation 25 (2), 236–245.

Dow, J.M., Neilan, R.E., Rizos, C., 2009. The international GNSS service in a changing landscape of global navigation satellite systems. J. Geodesy 83 (3), 191–198.

Du, S., Gao, Y., 2012. Inertial aided cycle slip detection and identification for integrated PPP GPS and INS. Sensors 12 (11), 14344–14362.

Gao, Z., Zhang, H., Ge, M., Niu, X., Shen, W., Wickert, J., Schuh, H., 2015. Tightly coupled integration of ionosphere-constrained precise point positioning and inertial navigation systems. Sensors 15 (3), 5783–5802.

Gao, Z., Zhang, H., Ge, M., Niu, X., Shen, W., Wickert, J., Schuh, H., 2016. Tightly coupled integration of multi-GNSS PPP and MEMS inertial measurement unit data. GPS Solutions 2016. http://dx.doi.org/10.1007/s10291-016-0527-z.

Ge, M., Gendt, G., Dick, G., Zhang, F.P., Reigber, C., 2005. Impact of GPS satellite antenna offsets on scale changes in global network solutions. Geophys. Res. Lett. 32 (6). http://dx.doi.org/10.1029/2004GL022224.

Ge, M., Gendt, G., Rothacher, M.A., Shi, C., Liu, J., 2008. Resolution of GPS carrier-phase ambiguities in precise point positioning (PPP) with daily observations. J. Geodesy 82 (7), 389–399.

Geng, J., Teferle, F.N., Meng, X., Dodson, A.H., 2011. Towards PPP-RTK: ambiguity resolution in real-time precise point positioning. Adv. Space Res. 47 (10), 1664–1673.

Gendt, G., Dick, G., Reigber, C.H., Tomassini, M., Liu, Y., Ramatschi, M., 2003. Demonstration of NRT GPS water vapor monitoring for numerical weather prediction in Germany. J. Meteorol. Soc. Jpn 82, 360–370.

Godha, S., 2006. Performance Evaluation of Low Cost MEMS-based IMU Integrated with GPS for Land Vehicle Navigation Application. Library and Archives Canada.

Kim, J., Jee, G.I., Lee, J.G., 1998. A complete GPS/INS integration technique using GPS carrier phase measurements. In: Position Location and Navigation Symposium. IEEE.

Kouba, J., 2009. A guide to using International GNSS Service (IGS) Products. Tech. rep., International GNSS Service. <http://acc.igs.org/UsingIGSProductsVer21.pdf>.

Li, X., Ge, M., Lu, C., Zhang, Y., Wang, R., Wickert, J., Schuh, H., 2014. High-rate GPS seismology using real-time precise point positioning with ambiguity resolution. IEEE Trans. Geosci. Remote Sens. 52 (10), 6165–6180.

Li, X., Ge, M., Zhang, X., Zhang, Y., Guo, B., Wang, R., Klotz, J., Wickert, J., 2013. Real-time high-rate co-seismic displacement from ambiguity-fixed precise point positioning: application to earthquake early warning. Geophys. Res. Lett. 40 (2), 295–300.

Lu, C., Li, X., Nilsson, T., Ning, T., Heinkelmann, R., Ge, M., Glase, S., Schuh, H., 2015. Real-time retrieval of precipitable water vapor from GPS and BeiDou observations. J. Geodesy 89 (9), 843–856.

Martin, J.C., George, L., 1981. Continuous state feedback guaranteeing uniform ultimate boundedness for uncertain dynamic systems. IEEE Trans. Autom. Control 26 (5), 1139–1144.

Odijk, D., Zhang, B., Teunissen, P.J., 2015. Multi-GNSS PPP and PPP-RTK: some GPS+ BDS results in Australia. China Satellite Navigation Conference (CSNC) 2015 Proceedings, vol. II. Springer, Berlin Heidelberg, pp. 613–623.

Pan, Z., Chai, H., Liu, Z., Yang, K., Chong, Y., Xu, Y., 2015. Integrating BDS and GPS to accelerate convergence and initialization time of precise point positioning. China Satellite Navigation Conference (CSNC) 2015 Proceedings, vol. III. Springer, Berlin Heidelberg, pp. 67–80.

Rabbou, M.A., El-Rabbany, A., 2015. Tightly coupled integration of GPS precise point positioning and MEMS-based inertial systems. GPS Solutions 19 (4), 601–609.

Roesler, G., Martell, H., 2009. Tightly coupled processing of precise point position (PPP) and INS data. In: Proceedings of the 22nd International Meeting of the Satellite Division of the Institute of Navigation, Savannah, GA, USA.

Savage, P.G., 2000. Strapdown Analytics. Strapdown Associates, Maple Plain, MN.

Schaer, S., Gurtner, W., Feltens, J., 1998. IONEX: The ionosphere map exchange format version 1. In: Proceedings of the IGS AC workshop, Darmstadt, Germany, vol. 9(11).

Scherzinger, B.M., 2000. Precise robust positioning with inertial/GPS RTK. In: Proceedings of the 13th International Technical Meeting for the Satellite Division of the Institute of Navigation (ION GPS).

Shin, E.H., 2006. Estimation Techniques for Low-Cost Inertial Navigation. Library and Archives Canada= Bibliothèque et Archives, Canada.

Steigenberger, P., Hauschild, A., Montenbruck, O., Hugentobler, U., 2012, July. Performance analysis of compass orbit and clock determination and compass-only PPP. In: IGS Workshop, pp. 23–27.

Tu, R., Ge, M., Zhang, H., Huang, G., 2013. The realization and convergence analysis of combined PPP based on raw observation. Adv. Space Res. 52 (1), 211–221.

Witchayangkoon, B., 2000. Elements of GPS Precise Point Positioning Doctoral dissertation. University of New Brunswick.

Yang, Y., Li, J., Xu, J., Tang, J., Guo, H., He, H., 2011. Contribution of the compass satellite navigation system to global PNT users. Chin. Sci. Bull. 56 (26), 2813–2819.

Zhang, H., Gao, Z., Ge, M., Niu, X., Huang, L., Tu, R., Li, X., 2013. On the convergence of ionospheric constrained precise point positioning (IC-PPP) based on undifferential uncombined raw GNSS observations. Sensors 13 (11), 15708–15725.

Zhang, X., Li, X., 2012. Instantaneous re-initialization in real-time kinematic PPP with cycle slip fixing. GPS Solutions 16 (3), 315–327.

Zhang, Y., Gao, Y., 2008. Integration of INS and un-differenced GPS measurements for precise position and attitude determination. J. Navigation 61 (01), 87–97.

Zhao, Q., Guo, J., Li, M., Qu, L., Hu, Z., Shi, C., Liu, J., 2013. Initial results of precise orbit and clock determination for COMPASS navigation satellite system. J. Geodesy 87 (5), 475–486.

Zumberge, J.F., Heflin, M.B., Jefferson, D.C., Watkins, M.M., Webb, F. H., 1997. Precise point positioning for the efficient and robust analysis of GPS data from large networks. J. Geophys. Res.: Solid Earth 102 (B3), 5005–5017.